spectrometer at 25°C in 50 mM NaCl and 10 mM sodium phosphate (pH 6.5). Data were obtained on complexes of unlabeled RNA and unlabeled peptide, unlabeled RNA and specific [^{15}N]glycine-containing peptide, and uniformly ^{13}C-labeled RNA and unlabeled peptide at concentrations of 1 to 2 mM. Initially, NMR spectra of the unlabeled complex were partially assigned from standard homonuclear and heteronuclear experiments. Complete assignment of all RNA nonexchangeable protons, and imino and amino protons in base-paired nucleotides, was achieved with a combination of SSNOESY [S. H. Smallcombe, *J. Am. Chem. Soc.* **115**, 4776 (1993)], constant-time HSQC [J. Santoro and G. King, *J. Magn. Reson.* **97**, 202 (1992)], 3D-HCCH-TOCSY and 3D-NOESY-HMQC [G. M. Clore *et al.*, *Biochemistry* **29**, 8172 (1990)], and ^{13}C-filtered NMR [G. Otting and K. Wüthrich, *Q. Rev. Biophys.* **23**, 39 (1990)] experiments (where HSQC is heteronuclear single-quantum coherence; TOCSY, total correlation spectroscopy; NOESY, nuclear Overhauser effect spectroscopy; and 3D, three-dimensional). Peptide assignments in the complex (all amide, α, and most side chain protons) were confirmed with peptides labeled with [^{15}N]glycine at positions 74 or 76. Assignments of the bulge nucleotides U10 and U12 in BIV TAR were confirmed by studies of the U12 deletion mutant. Distance restraints were obtained from NOESY with mixing times of 50 and 100 ms, with certain intermolecular restraints derived from 3D-NOESY-HMQC with a mixing time of 200 ms. Distance restraints were classified as strong (<2.5 Å), medium (<3.5 Å), or weak (<5.0 Å); appropriate pseudoatom corrections were applied for all nonstereospecifically assigned methylene groups. Dihedral torsion angle restraints were obtained from double-quantum–filtered correlation spectroscopy (DQF-COSY) experiments. Ribose conformations were restrained to be either C-3′-endo or C-2′-endo. Ribose sugars with mixed sugar conformations were not restrained. The phosphodiester torsion angles α and ζ were constrained loosely to adopt non-trans conformations, because of the absence of upfield shifted ^{31}P resonances. Other torsion angles in the RNA were not restrained.

15. Structures were calculated with a simulated annealing protocol within the InsightII NMRArchitect package (Biosym Technologies, San Diego, CA). A randomized array of atoms corresponding to peptide and RNA was heated to 1000 K, and bonding, distance, and dihedral restraints and a repulsive quartic potential were gradually increased to full value over 30 ps of molecular dynamics. The molecules were then cooled during 10 ps to 273 K and subjected to a final energy-minimization step that included an attractive Lennard-Jones potential. No electrostatic term was included in the target function. A total of 384 distance restraints were used, including 108 intranucleotide RNA restraints, 193 internucleotide RNA restraints, 30 hydrogen-bonding restraints in RNA, 27 intraresidue peptide restraints, 30 interresidue peptide restraints, and 26 RNA-peptide restraints; only conformationally significant restraints were included. A total of 76 experimental dihedral restraints were used, comprising eight peptide and 68 RNA restraints. Additional restraints were included to maintain chirality and peptide-bond planarity. The final force constants for distance, dihedral, and peptide-bond planarity restraints were 40, 60, and 200 kcal mol^{-1}, respectively. All color figures were generated with the program InsightII (Biosym Technologies). Experimental restraints as well as coordinates for the 20 final simulated annealing structures and the average energy-minimized structure will be deposited in the Brookhaven Protein Data Base.
16. J. D. Puglisi, data not shown. The U12 deletion mutant RNA–peptide complex yielded the same intramolecular and intermolecular NOEs as the wild-type complex.
17. Major groove width is defined as the phosphate-phosphate distance between G22 and G9. A canonical A-form helix was compared to the minimized average structure of the BIV TAR-peptide complex. The distance was measured from the center of mass of the phosphates, not considering van der Waals radii.
18. T. E. Creighton, *Proteins: Structures and Molecular Properties* (Freeman, New York, 1993). The turn is defined by a hydrogen bond between the Gly^{74} carbonyl group and the Arg^{77} amide nitrogen.
19. Peptide-RNA NOE restraints used in structure calculations included G14(H-1)–Arg^{70} (δ), C23(NH$_2$)–Arg^{70} (α, γ, δ), G22(H-8)–Gly^{71}(NH, α), G22(H-8)–Thr^{72}(β, Me), G22(H-3′)–Thr^{72}(Me), G22(H-5′/5″)–Thr^{72}(Me), C23(H-6)–Thr^{72}(Me), C23(H-5)–Thr^{72}(Me), C25(H-5)–Arg^{73}(γ, δ), C25(NH$_2$)–Arg^{73}(γ, δ), C23(H-5)–Gly^{74}(α), U24(H-5)–Gly^{74}(α), U24(H-3′)–Gly^{74}(α), U10(H-5)–Ile^{79}(γ, δ, β), G11(H-1)–Arg^{73}(δ), C26(NH$_2$)–Arg^{77}(α, γ, δ), C26(NH$_2$)–Arg^{77}(α, γ, δ), and G9(H-1)–Arg^{77}(δ). All contacts discussed in the text are constrained by direct NOE restraints.
20. K. M. Weeks and D. M. Crothers, *Biochemistry* **31**, 10281 (1992); *Science* **261**, 1574 (1993).
21. J. D. Puglisi, R. Tan, B. J. Calnan, A. D. Frankel, J. R. Williamson, *Science* **257**, 76 (1992); J. Tao and A. D. Frankel, *Proc. Natl. Acad. Sci. U.S.A.* **89**, 2723 (1992).
22. R. Tan, L. Chen, J. A. Buettner, D. Hudson, A. D. Frankel, *Cell* **73**, 1031 (1993); J. L. Battiste, R. Tan, A. D. Frankel, J. R. Williamson, *Biochemistry* **33**, 2741 (1994); R. D. Peterson, D. P. Bartel, J. W. Szostak, S. J. Horvath, J. Feigon, *ibid.*, p. 5357.
23. R. Tan and A. D. Frankel, *Proc. Natl. Acad. Sci. U.S.A.* **92**, 5282 (1995).
24. W. S. Somers and S. E. V. Phillips, *Nature* **359**, 387 (1992).
25. J. N. Breg, J. H. J. van Opheusden, M. J. M. Burgering, R. Boelens, R. Kaptein, *ibid.* **346**, 586 (1990); B. E. Raumann, M. A. Rould, C. O. Pabo, R. T. Sauer, *ibid.* **367**, 754 (1994).
26. W. Xu, M. A. Rould, S. Jun, C. Desplan, C. O. Pabo, *Cell* **80**, 639 (1995).
27. C. Y. King and M. A. Weiss, *Proc. Natl. Acad. Sci. U.S.A.* **90**, 11990 (1993); M. H. Werner, J. R. Huth, A. M. Gronenborn, G. M. Clore, *Cell* **81**, 705 (1995).
28. M. A. Schumacher, K. Y. Choi, H. Zalkin, R. G. Brennan, *Science* **266**, 763 (1994).
29. J. L. Kim, D. B. Nikolov, S. K. Burley, *Nature* **365**, 520 (1993).
30. Y. Kim, J. H. Geiger, S. Hahn, P. B. Sigler, *ibid.*, p. 512.
31. We thank E. V. Puglisi for helpful discussions and suggestions on the manuscript, R. Batey for helpful discussions, I. Tinoco Jr. for reading the manuscript, and H. Noller for encouragement. Supported by grants from the Dreyfus Foundation, the Packard Foundation (J.D.P.), and NIH (AI29135 to A.D.F.) as well as by NIH postdoctoral fellowship AI08591 (L.C.). The NMR facility is supported by a grant from the Markey Foundation to the Center for Molecular Biology of RNA at the University of California, Santa Cruz.

3 July 1995; accepted 22 September 1995

Inflammatory Bowel Disease and Adenomas in Mice Expressing a Dominant Negative N-Cadherin

Michelle L. Hermiston and Jeffrey I. Gordon*

Cadherins mediate cell adhesion and are essential for normal development. Embryonic stem cells were transfected with a dominant negative N-cadherin mutant (NCADΔ) under the control of promoters active in small intestinal epithelial cells and then introduced into C57BL/6 mouse blastocysts. Analysis of adult chimeric mice revealed that expression of NCADΔ along the entire crypt-villus axis, but not in the villus epithelium alone, produced an inflammatory bowel disease resembling Crohn's disease. NCADΔ perturbed proliferation, migration, and death programs in crypts, which lead to adenomas. This model provides insights about cadherin function in an adult organ and the factors underlying inflammatory bowel disease and intestinal neoplasia.

Precise control of cell adhesion is necessary during embryogenesis. In adult organisms, perturbations of cell adhesion are associated with tumor invasion and metastasis. Cadherins are transmembrane glycoproteins that mediate homophilic adhesive interactions between cells (*1*). Their conserved cytoplasmic domains interact with β-catenin or plakoglobin, which bind α-catenin (*2*). These interactions are essential for linkage to the actin cytoskeleton and for productive adhesion (*3*). Results from cell culture studies indicate that cadherin-catenin complexes regulate cell polarity, formation of junctional complexes, migration, and proliferation (*1*, *3*). Disruption of endogenous cadherin production results in embryonic lethality in mice and *Xenopus*, establishing the fundamental role of cadherins in development (*4*). We describe here the consequences of disrupting cadherin function in the crypt and villus epithelium of the adult mouse small intestine.

The mouse intestinal epithelium expresses a sequence of "developmental events"—proliferation, lineage allocation, migration, differentiation, and death—throughout life (*5*). Proliferation is confined to the crypts of Lieberkühn. The crypt's multipotent stem cell gives rise to enterocytes, mucus-producing goblet cells, enteroendocrine cells, and Paneth cells. Member cells of these four lineages differentiate during an orderly migration and are subsequently eliminated by apoptosis and exfoliation or phagocytosis. Renewal is rapid (3 to 20 days).

The organization of the small intestinal

Department of Molecular Biology and Pharmacology, Washington University School of Medicine, St. Louis, MO 63110, USA.

*To whom correspondence should be addressed.

epithelium makes it possible to use chimeric mice, generated from normal blastocysts and genetically manipulated embryonic stem (ES) cells, to study cadherin function (6). All stem cells in each crypt of an adult chimeric mouse share an identical genotype (7, 8). Each intestinal villus receives epithelial cells from several surrounding monoclonal crypts. Cells differentiate as they leave a crypt and migrate up an adjacent villus in a vertical coherent column. When 129/Sv ES cells are introduced into a normal B6 blastocyst, the resulting B6↔129/Sv intestine will contain patches of ES cell–derived crypt-villus units and patches of B6 crypt-villus units (6, 8). The ES cell patches are readily identifiable in whole-mount preparations of intestine because 129/Sv but not B6 enterocytes bind the lectin *Ulex europeaus* agglutinin type 1 (UEA1) (8) (Fig. 1A). The B6 patches act as internal controls to assess the effects of the genetic manipulation. Promoters are available to express wild-type or dominant negative mutant proteins at different positions along the crypt-villus and duodenal-ileal axes (5). By transfecting ES cells with these DNAs, we can confine manipulation of essential proteins such as the cadherins to a subpopulation of ES-derived epithelium in chimeras with a low percentage of 129/Sv contribution (6).

E-cadherin, the principal intestinal cadherin, is localized to the basolateral surfaces and apical junctional complexes of cells distributed along the length of crypt-villus units (6). Using a promoter that functions only in postmitotic villus enterocytes and a well-characterized dominant negative N-cadherin mutant lacking an extracellular domain (NCADΔ) (4), we previously determined that production of NCADΔ causes loss of endogenous E-cadherin from the cell surface, disruption of cell-cell and cell-matrix contacts, increased rates of cell migration, and precocious entry of enterocytes into a death program (6). We have now used a fatty acid binding protein gene (Fabp) promoter that is active in undifferentiated crypt epithelial cells and in differentiated members of all four lineages to express NCADΔ (9). The promoter's expression domain extends from the duodenum to the ileum, with maximal activity in the proximal jejunum (9). Embryonic stem cells were stably transfected with the Fabp promoter-NCADΔ DNA (10). Eight cloned ES cell lines were used to generate specific pathogen-free B6↔129/SvNCADΔ chimeras (10). Animals were examined at 1.5, 3, 6, 9, 12, or 19 months of age (n = two to six chimeras per ES cell line at each time point). Two cell lines yielded animals without any abnormalities, and six produced animals with similar intestinal phenotypes that were most pronounced in the proximal jejunum.

All chimeric mice generated from the six cell lines developed inflammatory bowel disease (IBD). Their small intestines contained patches of villi with poorly adherent UEA1$^+$ enterocytes (Fig. 1, B and C). Disruption of the epithelial barrier was associated with in-

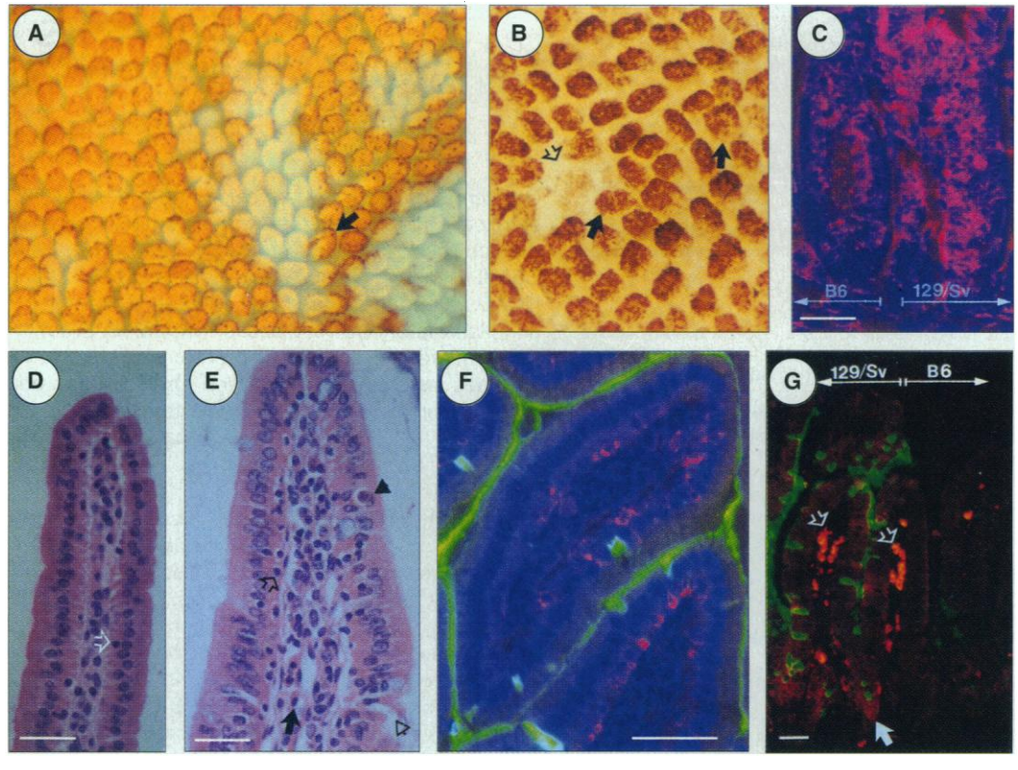

Fig. 1. Perturbed intestinal mucosal barrier in B6↔129/SvNCADΔ mice. (**A**) Whole-mount preparation of nontransgenic B6↔129/Sv jejunum stained with peroxidase-conjugated UEA1 (6). The arrow points to a polyclonal villus composed of columns of UEA1$^+$ epithelial cells (brown) from 129/Sv crypts and columns of UEA1$^-$ cells (white) from B6 crypts. (**B**) UEA1$^+$ region of B6↔129/SvNCADΔ jejunum showing a submucosal lymphoid aggregate (open arrow). By 6 months, the number of aggregates per small intestine was six times greater than in nontransgenic B6↔129/Sv cage mates (144 ± 5 versus 24 ± 2 in 50% 129/Sv chimeras; n = 6). The solid arrows point to villi with clear gaps between their epithelial cells, indicative of disrupted adhesion. Magnification in (A) and (B), ×60. (**C**) Section of jejunal crypts incubated with rabbit antibody to pancadherin (which recognizes the cytoplasmic domains of NCADΔ and endogenous cadherins), Cy3-donkey antibody to rabbit Ig, and bis-benzimide (blue nuclear stain) (10). The amount of NCADΔ expressed relative to endogenous cadherins can be determined by comparing the amounts of magenta staining in adjacent 129/Sv and B6 crypts. Immunostains with a monoclonal antibody to E-cadherin showed that NCADΔ production markedly depletes E-cadherin from the surfaces of 129/Sv crypt and villus epithelial cells (6, 12). (**D** and **E**) Hematoxylin and eosin–stained sections of proximal jejunal villi. UEA1 staining of serial sections confirmed that the villus in (D) was B6, and the villus in (E) was 129/Sv. The 129/SvNCADΔ villus has more IELs [open arrows in (D) and (E)], plasma cells [solid arrow in (E)], and apoptotic cells [solid arrowhead in (E)] and shows signs of cell adhesion defects [open arrowhead in (E)]. (**F**) 129/Sv jejunal villi sectioned perpendicular to their crypt-villus axis and stained with fluorescein isothiocyanate (FITC)–labeled UEA1 (green), rat antibody to mouse β_7 integrin (visualized with Cy3-donkey antibody to rat Ig), and bis-benzimide. β_7 integrin–positive IELs (red) are numerous. Because E-cadherin–$\alpha^E\beta_7$ interactions can mediate binding of T cells to cultured epithelial cells (21), this raises the possibility that alternative adhesion systems exist in the E-cadherin–depleted villus epithelium. (**G**) Boundary between 129/SvLNCADΔ and B6 patches in the proximal jejunum. The section was stained with FITC-UEA1, sheep antibody to mouse IgA, and Cy3-donkey antibody to sheep Ig (red-orange). The 129/Sv UEA1$^+$ villus (left) and the polyclonal villus located at the B6-129/Sv junction (middle) contain an increased number of IgA$^+$ cells in their lamina propria (open arrows) relative to B6 villi (right), and the amount of IgA is elevated in 129/Sv crypt epithelium (solid arrow). The abundance of IgA$^+$ [and IgG$^+$ (12)] plasma cells is consistent with B cell activation. Bars, 25 μm.

flammatory changes. By 6 weeks of age, the number and size of lymphoid aggregates was increased in 129/SvNCADΔ but not in B6 epithelium (Fig. 1B). Aggregates possessed germinal centers, peripheral $CD4^+\alpha\beta$ T cells, and an overlying epithelium with abundant antigen-sampling M cells (*11*, *12*). The lamina propria was expanded as a result of infiltration by lymphocytes, histiocytes, and immunoglobulin A (IgA)– and IgG-secreting plasma cells (Fig. 1, D, E, and G). The villus epithelium contained an enlarged population of β_7 integrin–positive intraepithelial lymphocytes (IELs) (Fig. 1F). Major histocompatibility complex (MHC) class II concentrations were markedly increased in epithelial cells distributed along crypt-villus units in 129/Sv but not in B6 patches (Fig. 2B).

By 3 months of age, mice developed histopathologic features of Crohn's disease, a type of human IBD (*13*). Foci of inflammation within 129/SvNCADΔ patches became transmural (Fig. 2A). Evident abnormalities included numerous lymphoid aggregates, lymphangiectasia, cryptitis, crypt abscesses characterized by a neutrophilic infiltrate, goblet cell depletion, Paneth cell hyperplasia, perturbed crypt-villus architecture, and aphthoid as well as larger linear mucosal ulcers (Fig. 2, C to G). Surveys of 1.5- to 19-month-old chimeras (n = 57) indicated that these histopathologic changes worsened progressively over the first year of life. The changes remained confined to the foci of 129/Sv ES cell–derived epithelium (Figs. 1F and 2, F and G), confirming the absence of an autoimmune disease. None of the histopathologic features were encountered in normal (nontransgenic) chimeras raised in the same microisolator, ruling out horizontal transmission of the IBD.

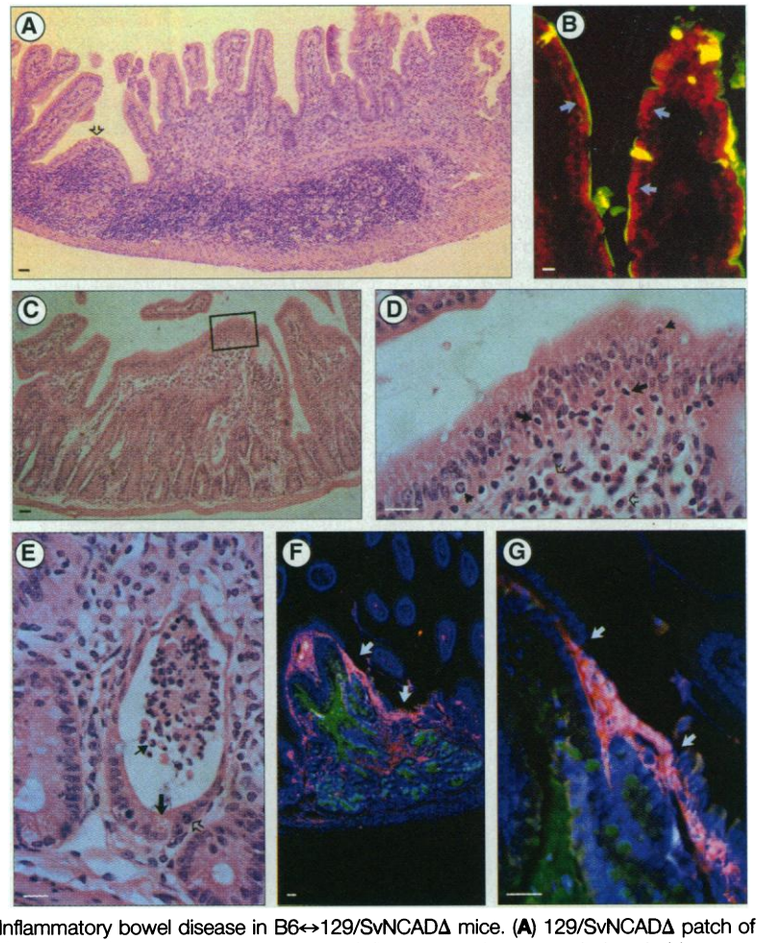

Fig. 2. Inflammatory bowel disease in B6↔129/SvNCADΔ mice. (**A**) 129/SvNCADΔ patch of jejunum from a 12-month-old mouse showing transmural inflammatory changes and a lymphoid aggregate (open arrow). (**B**) Jejunal section stained with FITC-UEA1 and rat antibody to MHC class II [visualized with Cy3-donkey antibody to rat Ig (red)]. High concentrations of MHC class II expression are evident in $UEA1^+$ villus enterocytes (arrows). (**C** and **D**) 129/Sv proximal jejunum showing inflammatory infiltrate with pronounced distortion of crypt-villus architecture. The boxed area in (C) is enlarged in (D). Numerous IELs (solid arrows), plasma cells (open arrows), and apoptotic cells (solid arrowheads) are evident in (D). (**E**) 129/Sv jejunal crypt showing an intraluminal abscess containing neutrophils (thin solid arrow) and cellular debris. The crypt epithelium is markedly flattened, disrupted in some areas, and contains apoptotic cells (open arrow). Paneth cells are present at the crypt base (thick solid arrow). The pericryptal lamina propria is infiltrated with plasma cells, lymphocytes, neutrophils, and macrophages. (**F**) 129/Sv ileal patch is stained as in Fig. 1G. Nuclei are visualized with bis-benzimide. Epithelial ulceration is evident (arrows). The epithelial breaches contain IgA (pink). The glandular structures (aqua) resemble the ulceration-associated cell lineage that develops in human intestine (*22*). (**G**) High-power view of the ulcerated region in (F). The arrows define the ulcer's margins. Bars, 25 μm.

Chimeras expressing NCADΔ along their entire crypt-villus axis were compared to chimeras that produced NCADΔ only in their villus epithelium. The mice were of similar age, had similar degrees of chimerism, were maintained together in microisolators, and had equivalent disruption of cell-cell and cell-matrix contacts on their villi. Animals that expressed only NCADΔ in their villus enterocytes had a limited mucosal immune response, even though clusters of bacteria were observed infiltrating between poorly adherent cells (6). There was a slight increase in lamina propria lymphocytes under 129/Sv villi and Peyer's patches were enlarged, but the histopathologic features of IBD were absent (*12*).

These results reveal differences in immune responsiveness along the crypt-villus axis. Vigorous immune responses to antigen penetration into $NCAD\Delta^+$ villi appeared to be suppressed. Entry of enteric antigens into normal villi may occur frequently because of perpetual apoptosis and cellular exfoliation, which creates a requirement for unresponsiveness. In contrast, antigen penetration through the crypt epithelium is associated with a robust immune response. Careful analyses of the distribution of immune mediators along crypt-villus units may provide information about the mechanisms that control responsiveness to normal enteric antigens (that is, oral tolerance).

A fundamental question about IBD is whether it reflects an appropriate response to an abnormal stimulus (for example, a pathogen or a weakened epithelial barrier) or an aberrant immune response to a normal stimulus (*14*). Knockouts of the T cell receptor (TCR) α, TCRβ, TCRβδ, MHC class II, interleukin-2 (IL-2), or IL-10 genes produce IBD in mice, presumably from a failure to suppress mucosal B cell responses to normal enteric antigens (*15*). The specific pathogen-free NCADΔ chimeras possess a complete repertoire of immune effectors. In these chimeras, IBD is initiated by a genetically engineered disruption of epithelial adhesion. We speculate that IBD may arise in immunocompetent individuals from functional disruptions of the crypt epithelium because of a variety of causes.

In addition to IBD, the chimeric mice developed intestinal neoplasms. By 6 weeks

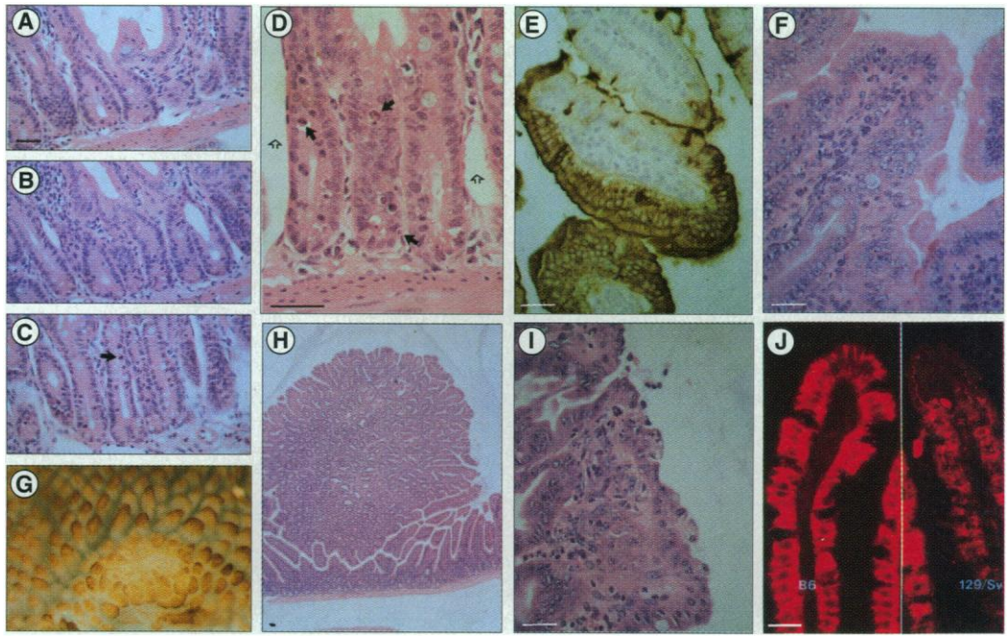

Fig. 3. Intestinal neoplasia in B6↔129/SvNCADΔ mice. (**A** to **C**) B6 crypts (A) and (B) and 129/SvNCADΔ crypts (C) from adjacent jejunal patches. NCADΔ production (Fig. 1C) is associated with hyperproliferation evidenced by an increase in the number of M-phase cells [arrow in (C)] and an increase in crypt depth. The B6 crypts in (B) are positioned at the B6-129/Sv boundary and show modest increases in depth compared with B6 crypts positioned in the middle of the patch (A), raising the possibility that enterotropic factors are produced by the 129/SvNCADΔ epithelium. (**D**) 129/SvNCADΔ jejunal crypts showing that proliferative abnormalities are accompanied by an increase in the number of apoptotic cells (solid arrows; independently confirmed by terminal deoxynucleotidyl transferase–mediated, deoxyuridine 5′-triphosphate–nick end labeling). Lymphangiectasia is apparent (open arrows). (**E**) Polyclonal jejunal villus sectioned perpendicular to its crypt-villus axis. A B6 villus and a 129/Sv villus are located at top and at bottom, respectively. UEA1$^+$ enterocytes (brown) are vacuolated and form multilayers. (**F**) 129/Sv jejunal villi with dysplastic epithelium. (**G**) UEA1-stained ileal whole mount showing an adenoma in a 129/Sv patch. (**H** and **I**) Hematoxylin and eosin–stained sections of UEA1$^+$ adenomas. High-power view (I) reveals enlarged, hyperchromatic nuclei with prominent nucleoli, increased mitotic activity, cell death, irregular surface infolding, and micropapillary tufts with secondary necrosis. These features distinguish the adenomas from inflammatory pseudopolyps. Like *Min* adenomas (*17*), most cells do not express markers of terminally differentiated enterocytes or of enteroendocrine, goblet, or Paneth cells (*12*). (**J**) Comparison of cellular concentrations and distribution of β-catenin in adjacent 129/SvNCADΔ and B6 jejunal villi. The section was incubated with rabbit antibody to β-catenin and Cy3-donkey antibody to rabbit Ig. Bar in (A), (D), (E), (F), (I), and (J), 25 μm; bar in (H), 50 μm. The same size bar as in (A) applies to (B) and (C).

of age, NCADΔ$^+$ crypts exhibited pronounced increases in proliferation and apoptosis when compared to adjacent B6 crypts, even in the absence of a surrounding inflammatory response (Fig. 3, A to D). Although immunostaining revealed differentiated members of all four lineages, there were signs of defective migration. UEA1$^+$ cells often formed multilayers in crypts and on villi (Fig. 3E). Mice derived from each of the six ES-NCADΔ cell lines developed foci of dysplasia within their 129/Sv epithelium (Fig. 3F). An analysis of chimeras generated from three ES cell lines revealed adenomas, distributed from the duodenum to the ileum (Fig. 3, G to I), beginning at 3, 6, and 9 months of age. Progression to adenocarcinoma was not observed during the first 19 months of life. Neoplastic changes were not found in the B6 patches of these animals, in comparably aged nontransgenic chimeras, or in mice that expressed NCADΔ only in their villus enterocytes (n = 184; ages from 1.5 to 19 months).

Results from previous studies have indicated that disruption of cadherin function is a late event in tumorigenesis (*16*). In our chimeras, tumorigenesis is initiated by perturbing endogenous cadherins in the crypt epithelium. Mutation of the adenomatous polyposis coli (APC) gene is an early event in the development of human colorectal neoplasms and produces small intestinal adenomas in *Min* mice (*17*). Catenin–E-cadherin complexes, catenin-APC complexes, and pools of free catenins exist in dynamic equilibrium within cells (*2*, *18*). By using NCADΔ to disrupt endogenous cadherins, we have affected this equilibrium, as evidenced by a reduction in the amounts and a change in the intracellular distributions of β-catenin (Fig. 3J) and E-cadherin (*6*). Our data are consistent with the notion that shifting the equilibrium toward catenin-APC complexes can increase proliferation, alter cell migration, and promote apoptosis. Added mutations affecting one or more of these processes could then lead to intestinal neoplasia.

Patients with IBD have an increased risk of developing intestinal neoplasms (*19*). The mechanisms responsible for this association are unknown. Components of the intestine's resident immune population can affect epithelial proliferation programs (*20*). However, mice with IBD from immunoregulatory gene knockouts do not develop gut neoplasms (*15*), and adenomas occurred in both inflamed and noninflamed 129/SvNCADΔ patches of chimeric intestine. Comparisons of normal B6 epithelium with inflamed or neoplastic 129/SvNCADΔ epithelium provide an opportunity to examine the pathogenesis of neoplasia in IBD.

REFERENCES AND NOTES

1. B. Ranscht, *Curr. Opin. Cell Biol.* **6**, 740 (1994); R. Kemler, *Trends Genet.* **9**, 317 (1993).
2. L. Hinck *et al.*, *J. Cell Biol.* **125**, 1327 (1994); I. S. Näthke *et al.*, *ibid.*, p. 1341.
3. A. Nagafuchi *et al.*, *ibid.* **127**, 235 (1994); M. Watabe *et al.*, *ibid.*, p. 247.
4. C. Kintner, *Cell* **69**, 225 (1992); E. Levine *et al.*, *Development* **120**, 901 (1994); L. Larue *et al.*, *Proc. Natl. Acad. Sci. U.S.A.* **91**, 8263 (1994).
5. J. I. Gordon and M. L. Hermiston, *Curr. Opin. Cell Biol.* **6**, 795 (1994).
6. M. L. Hermiston and J. I. Gordon, *J. Cell Biol.* **129**, 489 (1995).
7. G. H. Schmidt, D. J. Winton, B. A. J. Ponder, *Development* **103**, 785 (1988).
8. M. L. Hermiston, R. P. Green, J. I. Gordon, *Proc. Natl. Acad. Sci. U.S.A.* **90**, 8866 (1993).
9. J. F. Trahair *et al.*, *J. Cell Biol.* **109**, 3231 (1989); T. C. Simon *et al.*, *J. Biol. Chem.* **268**, 18345 (1993).
10. Nucleotides (nt) −596 to +21 of a rat fatty acid binding protein gene (*9*) were linked to nt +3 to +2150 of the human growth hormone (hGH) gene. A *pgk*-neomycin (*neo*) resistance selection cassette was placed downstream and in the same transcriptional orientation as hGH (*8*). *Xenopus* NCADΔC DNA (*4*) was introduced into the Bam HI site at nt +3 of hGH, which yielded LNCADΔ. LNCADΔ was transfected into D3 ES cells by means of electroporation. Single *neo*-resistant colonies were picked, amplified, and screened for LNCADΔ (*6*). Injection of 5 to 10 cells into B6 blastocysts produced viable B6↔129/SvNCADΔ chimeras, with 30 to 50% 129/Sv contribution to coat color. Animals were maintained in microisolator cages and given irradiated rodent chow (Pico Lab Rodent Diet 20, PMI Feeds, St. Louis, MO). Routine screens for pathogens were negative.
11. Immunohistochemical protocols, lectins, and antibodies were as described (*6*). Additional antisera

included goat antibody to rat CD4, CD8, and F480; hamster antibody to mouse TCRαβ and TCRγδ (PharMingen); rat antibody to mouse β_7 integrin (PharMingen); sheep antibody to mouse IgA (Sigma); donkey antibody to mouse IgG (Jackson ImmunoResearch); rat antibody to MHC class II (OX-3; Serotec); and rabbit antibody to β-catenin (*2*).
12. M. L. Hermiston and J. I. Gordon, unpublished observations.
13. R. H. Riddell, in *Inflammatory Bowel Disease*, J. B. Kirsner and R. G. Shorter, Eds. (Williams & Wilkins, Baltimore, ed. 4, 1995), pp. 517–552.
14. D. K. Podolsky, *N. Engl. J. Med.* **325**, 928 (1991).
15. P. Mombaerts *et al.*, *Cell* **75**, 275 (1993); B. Sadlack *et al.*, *ibid.*, p. 253; R. Kühn *et al.*, *ibid.*, p. 263.
16. W. Birchmeier and J. Behrens, *Biochim. Biophys. Acta* **1198**, 11 (1994).
17. L.-K. Su *et al.*, *Science* **256**, 668 (1992); A. R. Moser, W. F. Dove *et al.*, *J. Cell Biol.* **116**, 1517 (1992).
18. B. Rubinfeld *et al.*, *Science* **262**, 1731 (1993); L.-K. Su *et al.*, *ibid.*, p. 1734; B. Rubinfeld *et al.*, *J. Biol. Chem.* **270**, 5549 (1995).
19. B. Levin, in (*13*), pp. 461–473.
20. H. Komano *et al.*, *Proc. Natl. Acad. Sci. U.S.A.* **92**, 6147 (1995).
21. K. L. Cepek *et al.*, *Nature* **372**, 190 (1994).
22. N. A. Wright, C. Pike, G. Eli, *ibid.* **343**, 82 (1990); D. J. Ahnen *et al.*, *J. Pathol.* **173**, 317 (1994).
23. We thank D. O'Donnell for technical assistance, P. Swanson for reviewing the histopathology, E. Unanue for goat antibody to rat CD4, CD8, and F480, W. J. Nelson for antibody to β-catenin, and C. Kintner for pSP72NCADΔC. Supported in part by NIH grants DK39760 and DK30292.

11 July 1995; accepted 20 September 1995

Concerted Signaling by Retinal Ganglion Cells

Markus Meister,* Leon Lagnado,† Denis A. Baylor

To analyze the rules that govern communication between eye and brain, visual responses were recorded from an intact salamander retina. Parallel observation of many retinal ganglion cells with a microelectrode array showed that nearby neurons often fired synchronously, with spike delays of less than 10 milliseconds. The frequency of such synchronous spikes exceeded the correlation expected from a shared visual stimulus up to 20-fold. Synchronous firing persisted under a variety of visual stimuli and accounted for the majority of action potentials recorded. Analysis of receptive fields showed that concerted spikes encoded information not carried by individual cells; they may represent symbols in a multineuronal code for vision.

Current understanding of how the retina transmits the visual scene to the brain is based primarily on electrical recordings from single neurons. As a consequence, the spike trains from different optic nerve fibers have commonly been treated as independent messages about the environment. However, pairwise recordings from retinal ganglion cells in goldfish (*1*), rabbits (*2*), and cats (*3–5*) have shown that this assumption is violated—nearby cells of similar functional type have a strong tendency to fire synchronously. These measurements were all obtained in darkness or under constant uniform illumination [but see (*6*)], when ganglion cells fire sporadically, and thus it was not possible to assess the function of such correlations in visual signaling. It has been suggested that synchronous firing during visual stimulation would imply redundancy among neuronal messages and thus an inefficient use of the optic nerve (*2*).

To assess the importance of concerted firing in visual signaling, we used a microelectrode array to record simultaneously the spike trains of 30 to 50 ganglion cells in an isolated salamander retina (*7*). This preparation contains large hardy neurons and has been used extensively to study the cellular mechanisms of retinal processing. Figure 1A illustrates the responses of two nearby neurons to spatially uniform illumination that regularly switched between two intensity levels. Although each cell fired only a few spikes per stimulus period, at times that varied by several hundred milliseconds from trial to trial, the spikes from the two cells appeared to be tightly locked to each other in time. The mean firing rate of each neuron was strongly modulated by the periodic stimulus (Fig. 1B), and as a result, the correlation function between the two spike trains showed a pronounced periodic component (Fig. 1C). However, this stimulus-induced correlation was dwarfed by a tall peak near zero delay, with a full width at half maximum of only 20 ms (Fig. 1D). This strong tendency to fire in near-synchrony shows that the two neurons did not respond to light independently.

To quantify the strength of concerted firing, action potentials from cells 1 and 2 were defined as a spike pair if they occurred within 20 ms of each other. We then computed a correlation index as the number of spike pairs observed divided by the number expected if the two neurons responded independently (*8*). For the cell pair in Fig. 1, this index was 12.4, so that tightly linked pairs of spikes occurred about 12 times more frequently than was expected. Such anomalous pairing accounted for 60% of all spikes generated by cell 1 and 42% of spikes generated by cell 2. We computed correlation functions for all pairs among 32 cells in this retina: 31% of the pairs showed clear evidence of concerted firing, with a correlation peak near zero delay whose shape was similar to that shown in Fig. 1D, though it varied in amplitude. Further statistical analysis revealed that synchronous firing events generally extended over more than two neurons (*9*). Overall, these patterns of concerted firing accounted for approximately 50% of all action potentials from the recorded sample of ganglion cells. Because the electrode array typically monitored only 10% of the overlying ganglion cells, we probably missed many synchronous firing patterns. Thus, the fractional contribution of concerted firing to the retinal output may well exceed 50%.

The correlation index varied with the distance between the two neurons' receptive fields (Fig. 2). It decreased from a maximum of 20 at short distances by a factor of *e* over 200 μm. In comparison, the centers of these neurons' receptive fields had approximately Gaussian-shaped profiles (*10*), with an average radius of 120 μm. Concerted firing thus appears to be associated with overlap of receptive-field centers. At distances between 400 and 1000 μm, the correlation index dropped significantly below 1, indicating that more distant cells avoided firing together. When separated by more than 1000 μm, ganglion cells appeared to signal independently as assessed by this test. When the ganglion cells were sorted by functional type (*10*), it was found that pairs of "fast OFF" cells (Fig. 2A) exhibited more synchronous firing than did pairs of "slow OFF" cells (Fig. 2B), whereas pairs of ON cells produced the weakest correlation index (Fig. 2C). ON and OFF cells generally fired independently of each other, although some pairs with strong correlations were found at short distances (Fig. 2D). The shape of the correlation function (Fig. 1D) and its dependence on overlap of receptive fields (Fig. 2), as well as the dominance of synchronous firing among neurons with transient responses (Fig. 2A), are remarkably similar to the observations of Mastronarde (*3*) on cat ganglion cells under uniform illumination. In contrast to that study, we generally did not observe a sharp well in the cross-correlogram between an ON cell and an OFF cell. Furthermore, the negative correlation among cells of the same class at distances greater than 400 μm has not been reported previously.

M. Meister, Department of Molecular and Cellular Biology, Harvard University, 16 Divinity Avenue, Cambridge, MA 02138, USA. E-mail: meister@biosun.harvard.edu
L. Lagnado and D. A. Baylor, Department of Neurobiology, Sherman Fairchild Science Building, Stanford University School of Medicine, Stanford, CA 94305-5401, USA.

*To whom correspondence should be addressed.
†Present address: Medical Research Council Laboratory of Molecular Biology, Hills Road, Cambridge CB22QH, UK.